crystals

MDPI

Article

Influence of Ionic Liquids on the Functionality of Optoelectronic Devices Employing $CsPbBr_3$ Single Crystals

Faisal Alresheedi

Department of Physics, College of Science, Qassim University, Buraidah 51452, Saudi Arabia; f.alresheedi@qu.edu.sa

Abstract: Regulating the nucleation temperature and growth rates during inverse temperature crystallization (ITC) is vital for obtaining high-quality perovskite single crystals via this technique. Precise control over these parameters enables growing crystals optimized for various optoelectronic devices. In this study, it is demonstrated that incorporating a 1-butyl-3-methylimidazolium bromide (BMIB) ionic liquid into the precursor solution of cesium lead bromide ($CsPbBr_3$) brings about a dual enhancement effect. This includes a reduction in nucleation temperature from 85 °C to 65 °C and a significant improvement in both optoelectronic characteristics and crystal properties. The $CsPbBr_3$ single crystals grown using ITC with BMIB added (method (2)) demonstrate improved chemical and physical properties (crystallinity, lattice strain, nonradioactive recombination, and trap density) compared to $CsPbBr_3$ single crystals produced through conventional 85 °C ITC alone (method (1)). The exceptional quality of $CsPbBr_3$ single crystals produced with the inclusion of BMIB allowed for the development of a highly responsive optoelectronic device, demonstrating heightened sensitivity to green light. The findings of this investigation reveal that the growth of perovskite single crystals assisted by ionic liquid exerts a substantial impact on the characteristics of the crystals. This influence proves advantageous for the development of optoelectronic devices based on single crystals.

Keywords: carrier dynamics; perovskite; crystallization; crystal structure; optics

Citation: Alresheedi, F. Influence of Ionic Liquids on the Functionality of Optoelectronic Devices Employing $CsPbBr_3$ Single Crystals. *Crystals* **2024**, *14*, 956. https://doi.org/10.3390/cryst14110956

Academic Editor: Limei Zheng

Received: 4 October 2024
Revised: 21 October 2024
Accepted: 28 October 2024
Published: 31 October 2024

1. Introduction

The recent surge in research on metal halide perovskites (MHPs) stems from their exceptional properties and ease of fabrication, making them highly promising candidates for next-generation optoelectronic devices [1–4]. MHPs boast several attractive features, including efficient carrier mobility, tunable bandgaps, high light-absorption coefficients, broad light-absorption spectra, and straightforward synthesis methods [5–7]. $CsPbX_3$ (X = Cl, Br, I) all-inorganic halide perovskites stand out within the perovskite family due to their exceptional environmental stability, complementing their well-established optical properties. This combination makes them strong contenders for future optoelectronic applications [8–10]. Photodetectors play a critical role in various technologies by capturing incoming light signals and instantaneously converting them into electrical signals [11]. This functionality makes them crucial active components for applications in biomedical sensing, optical communication, advanced imaging, and environmental monitoring [12]. Therefore, numerous $CsPbX_3$-based photodetectors have been explored and demonstrate remarkable detection capabilities and potential for practical applications [13–15].

Researchers have explored a range of solution-based techniques for cultivating high-quality MHP single crystals [16,17]. These methods include antisolvent vapor-assisted crystallization, slow evaporation, the top-seed solution method, and ITC. This diversity allows for the growth of crystals with varying compositions and morphologies [17]. The ITC technique stands out for its ability to rapidly produce high-quality, well-defined perovskite single crystals within minutes [18]. This method leverages the concept of reduced solubility at elevated temperatures in different solutions to achieve control over

crystal growth. While the ITC method facilitates rapid crystal growth at high temperatures, this can also result in the formation of smaller crystals that may compromise overall quality [18]. Interestingly, these smaller crystals can act as seeds, promoting the subsequent growth of larger single crystals. The scientific community has extensively adopted a seed-assisted growth approach to achieve larger, high-quality MHP single crystals. This technique leverages smaller crystals as seeds to promote the formation of bigger crystals with superior characteristics [19]. In our earlier research, we introduced a seed-assisted ITC method that successfully reduced the $CsPbBr_3$ crystal growth temperature from 85 °C to 70 °C [20]. This innovation using lower temperatures alongside seed crystals positively impacted the optical properties and photodetector performance of the resulting $CsPbBr_3$ single crystals [20].

The two-step crystallization process inherent to the seed-assisted ITC method can be a drawback due to its complexity and cost implications [21,22]. As an alternative approach, researchers have explored manipulating the crystallization environment to achieve high-quality, large MHP single crystals efficiently at lower temperatures [21,22]. Modifying the perovskite precursor solution offers a promising strategy for achieving high-quality single crystals. For instance, incorporating formic acid or 3-(decyldimethylammonio)-propane-sulfonate inner salt can induce rapid growth in crystals with minimal defects [23–25]. This approach, compared to the seed-assisted ITC method, streamlines the process by eliminating the need for additional steps at lower temperatures. Studies have shown that incorporating ionic liquids into the perovskite precursor solution enhances the material's tendency to crystallize, leading to the formation of high-quality polycrystalline perovskite films with minimal defects [26,27]. Ionic liquids, with their unique combination of anions and cations, can interact strongly with perovskite precursors in solution through hydrogen bonding and coordination bonds. This interaction likely influences the crystallization process; however, their application in precisely controlling the growth of MHP single crystals remains unexplored, as evidenced by a lack of reported research in this area [26,27].

This study investigates the influence of one BMIB ionic liquid on $CsPbBr_3$ crystal growth. Our findings reveal that incorporating BMIB into the $CsPbBr_3$ precursor solution offers a promising route for achieving high-quality single crystals. Notably, this approach also facilitates a significant reduction in the nucleation temperature, from 85 °C to 65 °C. The investigation began by examining how different BMIB concentrations within the $CsPbBr_3$ precursor solution influence the nucleation time of $CsPbBr_3$ single crystals. Our study suggests that incorporating an optimal concentration of BMIB ionic liquid promotes a self-assembly and crystallization process. This effect likely arises from the formation of $PbBr_2$-BMIB complexes, which influence the crystallization pathway to favor the growth of larger single crystals. X-ray diffraction analysis indicated a significant difference in lattice strain between $CsPbBr_3$ single crystals. Crystals grown with BMIB exhibited lower lattice strain compared to those obtained using the traditional ITC method at 85 °C. $CsPbBr_3$ single crystals grown with BMIB displayed superior optical and electrical properties compared to those produced using the conventional ITC method. This finding further reinforces the high quality of BMIB-based crystals and their suitability for photodetector applications. Our research demonstrates that a planar-structured photodetector utilizing a BMIB-based $CsPbBr_3$ single crystal achieves a remarkable responsivity of 5.37 A W^{-1} and an external quantum efficiency (EQE) of 0.97 under green light (530 nm) at a bias voltage of 2 V. The responsivity and EQE achieved by our BMIB-based $CsPbBr_3$ photodetector significantly surpass those measured in devices fabricated using $CsPbBr_3$ single crystals grown by the conventional ITC method at 85 °C.

2. Materials and Methods

2.1. Materials

This research employed commercially available cesium bromide, lead (II) bromide, N,N-dimethylformamide, and BMIB (Sigma-Aldrich, Bayswater VIC, Australia) without further purification.

2.2. Synthesis

The $CsPbBr_3$ precursor solution was prepared by dissolving equimolar amounts of CsBr and $PbBr_2$ in DMF solvent. The mixture was then agitated using a vortex shaker at room temperature to achieve complete dissolution. The $CsPbBr_3$ precursor solution was then filtered using a 0.2 µm PTFE filter to remove any impurities. Next, the filtered solution was loaded into an oil bath and heated at a controlled rate of 5 °C per hour to reach a final temperature of 85 °C. This process was specifically designed to promote nucleation and crystal growth, with the onset of nucleation inferred based on the solution's behavior during heating. The controlled heating conditions allowed for accurate determination of the nucleation time. After the initial formation of crystals (nucleation), the solution was left undisturbed for roughly 5 h to allow the $CsPbBr_3$ single crystal to grow and mature. This resulted in crystals with approximate dimensions of $7 \times 7 \times 2$ mm^3.

The influence of different BMIB ionic liquid (IL) concentrations on $CsPbBr_3$ synthesis was investigated. The experiment explored a range of BMIB IL additions: 1 (corresponding to 31 mg), 3 (82 mg), 6 (129 mg), and 10 mol% (258 mg) relative to a 10 mL, 1.2 M $CsPbBr_3$ precursor solution. Following precursor preparation, the solution underwent filtration using a 0.2 micrometer PTFE filter to eliminate impurities. Subsequently, it was distributed into separate vials (four in total) and subjected to gradual heating, reaching a final temperature of 65 °C. After a 12 h period, this process yielded large single crystals exceeding $7 \times 7 \times 2$ mm^3 in size. These crystals were then dried and prepared for further characterization.

2.3. Devices

The (100) facets of the single crystals were equipped with a 60-nanometer-thick platinum (Pt) electrode. This process utilized a sputtered magnetron system and a custom-designed mask featuring a 150-micrometer channel for precise electrode placement.

2.4. Characterizations

The crystallographic properties of the samples were analyzed using micro-beam X-ray diffraction (XRD) equipment (D8 Discover, Bruker, MA, USA). The analysis employed Cu Kα-Irradiation with a tube voltage of 40 kV and a current of 40 mA.

Photoluminescence (PL) characteristics, including steady-state and time-resolved photoluminescence (TRPL) behavior, were investigated using an Edinburgh Instruments FLS 920 PL spectrometer equipped with a 450 nm excitation source and a modulation frequency of 5 MHz.

To characterize the space-charge limited current (SCLC) behavior, vertical devices were fabricated. This involved depositing Pt electrodes onto the top and bottom faces of the crystal using a sputtering technique. Current–voltage (I-V) measurements were performed with a Keithley 6517B electrometer, sweeping the voltage from 0 to 10 V in 25 mV steps. Each voltage step was followed by a short pulse (20 ms) and a long relaxation period (2 min) at 0 V.

Characterization of the devices under dark conditions (J-V) and their photodetector response involved a LASC probe station interfaced with a Bio-Logic SP-150e potentiostat. Light intensity from a green LED was optimized using a Thorlabs GmbH PM100D power meter.

3. Results and Discussion

$CsPbBr_3$ single crystals were synthesized using method (1), which has been documented in a prior publication [20]. In the process of conventional nucleation growth, the $CsPbBr_3$ precursor solution was prepared by dissolving CsBr and $PbBr_2$ in equimolar amounts in DMF. The initiation of the nucleation process took around 30 min at a temperature of 85 °C. Subsequently, single crystals with the targeted dimensions of approximately $7 \times 7 \times 2$ mm^3 were noted following a continuous crystallization period of 5 h, as depicted in Figure 1a,b. The crystallization process of the $CsPbBr_3$ precursor solution was additionally examined at a reduced temperature of 65 °C. Nevertheless, even after a day, the absence

of $CsPbBr_3$ single crystals was noted at this particular temperature. This corresponds with information found in published works, where it is reported that achieving the required level of supersaturation for the nucleation and growth of a perovskite single crystals at a lower temperature of 65 °C typically takes approximately 18 days [28].

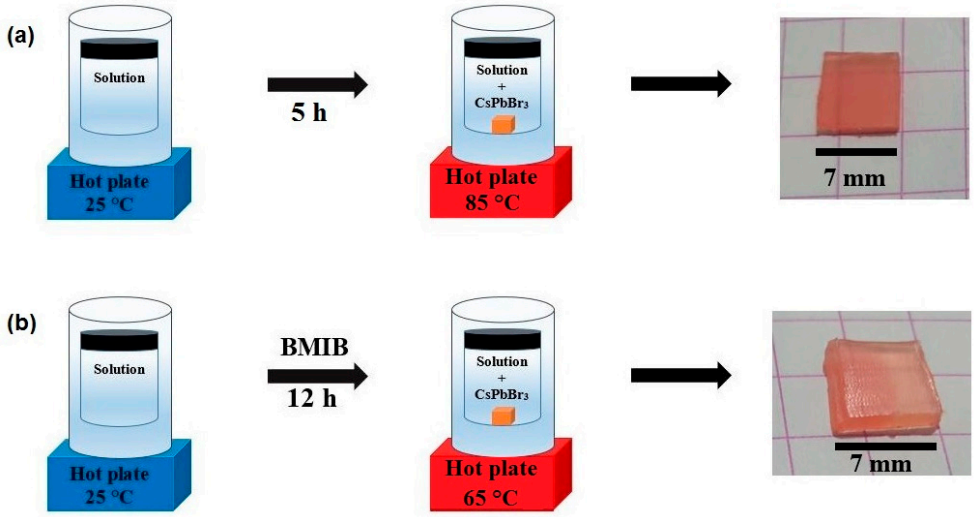

Figure 1. Diagram illustrating the synthesis of $CsPbBr_3$ single crystal under two conditions: (**a**) without BMIB and (**b**) with the addition of BMIB.

In the synthesis process involving the ionic liquid additive, the $CsPbBr_3$ precursor solution was supplemented with BMIB at different conditions (1, 3, 6, and 10 mol%). The crystallization temperature was established at 65 °C with a heating rate of 10 °C per hour. The duration of nucleation (after reaching 65 °C) exhibited variability corresponding to the incremental rise in BMIB concentration (Table 1). Observations revealed the successful formation of $CsPbBr_3$ single crystals with the intended dimensions. These crystals were derived from the precursor solution containing 6 mol% BMIB and underwent growth for a duration of 12 h. When employing lower BMIB concentrations (1 mol% and 3 mol%), the resulting outcome after a 12 h period was the formation of minute crystallites, attributable to the notably sluggish rate of crystallization. Nevertheless, elevating the BMIB concentration to 10 mol% proved ineffective in inducing nucleation at the temperature of 65 °C.

Table 1. Investigating nucleation and growth kinetics of CsPbBr3 single crystals.

Procedures	Nucleation Duration	Temperature	Single Crystal Type/ Growth Duration
Reference	0.5 h	85 °C	Large/5 h
With BMIB (1 mol%)	4 h	65 °C	Small/24 h
With BMIB (3 mol%)	5 h	65 °C	Small/24 h
With BMIB (6 mol%)	1.5 h	65 °C	Large/12 h
With BMIB (10 mol%)	N/A	65 °C	NA/12 h

The development of single crystals is commonly regulated by both the solute's diffusion rate within the solution and the deposition rate of the solute onto the crystal surface [29]. As per Equation (1), the diffusion rate within the solution experiences exponential growth as the temperature rises [20].

$$D = D_0 e^{(-\frac{\Delta H}{RT})} \quad (1)$$

The symbols in this equation maintain their conventional meanings and interpretations.

Hence, elevated temperatures (85 °C) may result in a heightened diffusion rate, potentially causing the development of single crystals harboring flaws and irregularities [30,31].

To maintain optimal crystal growth quality at lower temperatures, a critical balance between the diffusion rate and the rate of solute deposition needs to be achieved. Incorporating 6% BMIB into the $CsPbBr_3$ precursor solution proved instrumental in surmounting the nucleation energy barrier for nucleus formation at the relatively low temperature of 65 °C. This addition facilitated the growth of crystals while remaining within the supersaturation threshold. For a more in-depth examination of the impact of 6 mol% BMIB on the rate of crystallization, we undertook the crystallization process of $CsPbBr_3$ single crystals both with and without the inclusion of the BMIB additive, conducted at a temperature of 85 °C. The initiation of the nucleation process took approximately 1 h for the precursor solution containing BMIB, significantly exceeding the nucleation time observed for the precursor solution lacking BMIB. The extended duration of the nucleation process in the precursor solution containing BMIB can be ascribed to the interactions between BMIB and the perovskite component. These interactions impede ion diffusion, consequently influencing the growth rate of $CsPbBr_3$ single crystals. For assessing the crystallization rate, we extended the crystallization process by an additional 6 h post-nucleation. As outlined in Table 2, incorporating BMIB into the perovskite solution diminishes the growth rate, providing a means to regulate the formation of single crystals during the ITC method. The introduction of BMIB has the potential to impact the crystal growth kinetics of $CsPbBr_3$ single crystals, consequently influencing the crystal features.

Table 2. Crystal growth rate of CsPbBr3.

Procedures	Nucleation Duration	Single Crystal Weight (6 h)	Mean Rate of Increase
Reference	0.5 h	402 mg	0.96 mg/min
With BMIB (6 mol%)	1 h	347 mg	0.71 mg/min

To validate this, we initially examined the presence of BMIB in both the bulk and on the surface of $CsPbBr_3$ single crystals using liquid-state ^1H nuclear magnetic resonance (NMR) measurements. As shown in Figure 2a, the lack of characteristic signals of BMIB in the respective NMR spectra indicates that this additive does not exist in the crystalline framework. Nevertheless, interactions between BMIB molecules and the lead(II) bromide entity in the precursor solution may occur through hydrogen bonding, potentially impacting the solidification progression by diminishing the solute dissemination pace [32].

The ^1H NMR spectrum presented in Figure 2b depicts the outcome of the direct reaction between BMIB and lead(II) bromide in a molar ratio of 1:1. Observed in the spectrum, the peak corresponding to BMIB at 9.16 ppm undergoes a shift towards the high field region, registering at 9.09 ppm post the introduction of $PbBr_2$. This shift implies the creation of the $[BMI]PbBr_3$ salt [32].

The X-ray diffractograms of the predominant facet for both $CsPbBr_3$ single crystals displayed distinctive peaks along the different planes, substantiating their elevated purity, as evidenced in Figure 3. However, the significantly increased intensities of these peaks in method (2) imply enhanced crystal quality. Moreover, the examination of the full width at half-maximum (FWHM) for the three principal peaks allows the assessment of lattice strain through the application of the tangent formula (refer to Supplementary Note 1) [20,32]. Table 3 outlines the FWHM and lattice strain values for both methods. Notably, method (2) demonstrates a lower FWHM, indicating a decrease in lattice strain within the $CsPbBr_3$ single crystal. The lessened lattice strain offers advantages by diminishing the migration of ions within the $CsPbBr_3$ single crystal and reducing the nonradiative recombination operation [33].

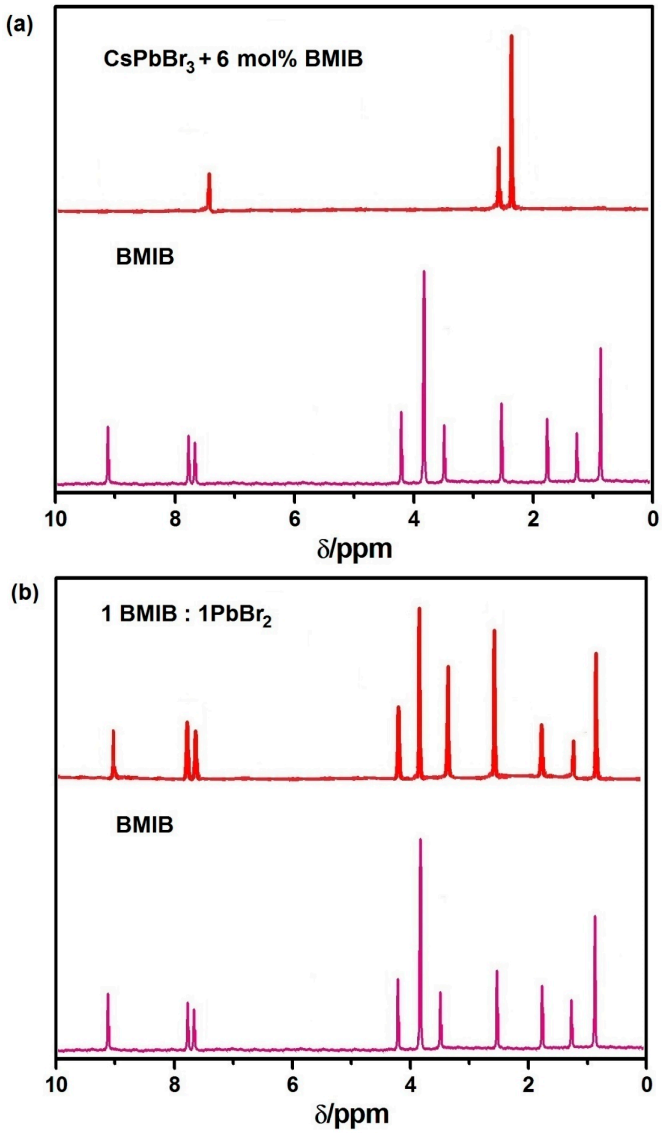

Figure 2. (**a**) Comparative ^{1}H NMR analysis of BMIB and $CsPbBr_3$ crystals with incorporated BMIB. (**b**) ^{1}H NMR analysis of BMIB and its interaction with $PbBr_2$ in DMSO-d_6.

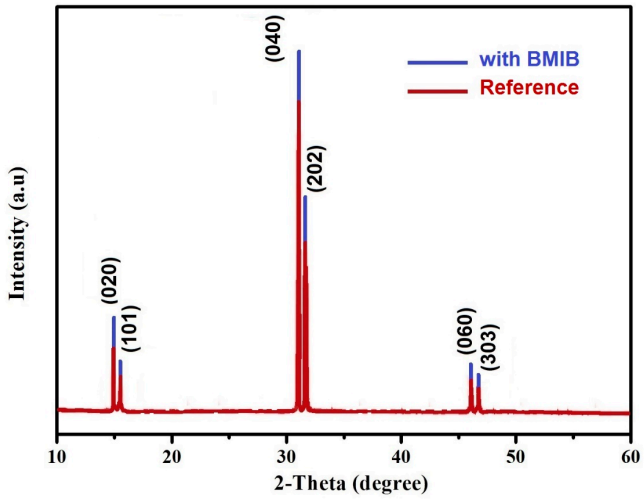

Figure 3. Room temperature XRD patterns of $CsPbBr_3$ single crystals.

Table 3. Impact of BMIB incorporation on lattice strain in CsPbBr3 single crystals.

	FWHM (°)		L_s (%)	
Miller Indices (hkl)	**With BMIB**	**Reference**	**With BMIB**	**Reference**
(020)	0.054	0.063	0.074	0.120
(101)	0.041	0.048	0.047	0.095
(040)	0.082	0.096	0.108	0.179
(202)	0.089	0.103	0.132	0.184
(060)	0.034	0.042	0.019	0.041
(303)	0.019	0.033	0.018	0.037

The trap states situated within the band gap of halide compounds act as crucial impediments in various photonic usages [34]. In order to gain further insights into the characteristics and imperfections, PL assessments were conducted on both categories of $CsPbBr_3$ single crystals. Illustrated in Figure 4, the PL spectra demonstrate a well-defined peak at 517 nm without any alteration in the peak position, aligning with what is reported in the existing literature [20]. Significantly, the $CsPbBr_3$ single crystal, synthesized using method (2), demonstrated an increased PL intensity when compared to the single crystal prepared through method (1). This enhancement suggests the mitigation of nonradiative recombination in the modified $CsPbBr_3$ single crystal. However, we acknowledge that the intensity of photoluminescence (PL) depends not only on the quantum yield but also on the amount of absorbed light, which is influenced by factors such as sample thickness, surface quality, and scattering effects. The difference in intensity at the PL maximum of 10–20% could easily be attributed to these phenomena. It is quite possible that if the PL spectra of different samples grown under identical conditions were compared, a similar pattern would be observed. These outcomes provide additional backing for our observations derived from the X-ray diffraction examination.

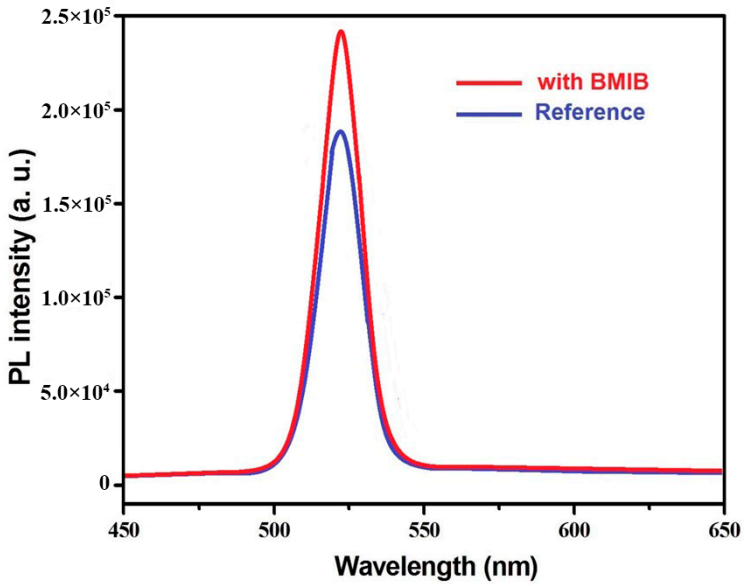

Figure 4. Photoluminescence characterization of emission properties in different $CsPbBr_3$ single crystals (RT).

Subsequently, we delved into the exploration of the charge transmission and electronic attributes of these semiconductors, employing the SCLC technique [35]. The dark current of the vertically structured Pt/$CsPbBr_3$/Pt devices (Figure 5a), designed to allow only hole transport, was recorded. Through this process, we determined the values of conductivity (σ), trap density (η_{trap}), and mobility (μ). To mitigate the influence of ion migration during the measurement process, we employed the pulsed voltage sweep SCLC method. The

dark current–voltage (I-V) characteristics of both $CsPbBr_3$ single crystals are presented in Figure 5b. Upon examination of both dark current–voltage (I-V) curves, three distinct regions can be identified: ohmic, trap-filling, and Child regions. By analyzing the ohmic region, we calculated the conductivity (σ) for both single crystal types. The $CsPbBr_3$ single crystal synthesized using method (2) demonstrates a higher conductivity value compared to the reference $CsPbBr_3$ single crystal (Figure 6a). In the context of the trap-filling region and assuming a linear relationship, the relationship between trap density (η_{trap}), the hole densities (η_h), and the trap-filled limit voltage (V_{TFL}) can be determined through Equation (2) [20]:

$$n_{trap} = \frac{2\varepsilon\varepsilon_0 V_{TFL}}{eL^2} \quad (2)$$

The symbols in this equation maintain their conventional meanings and interpretations.

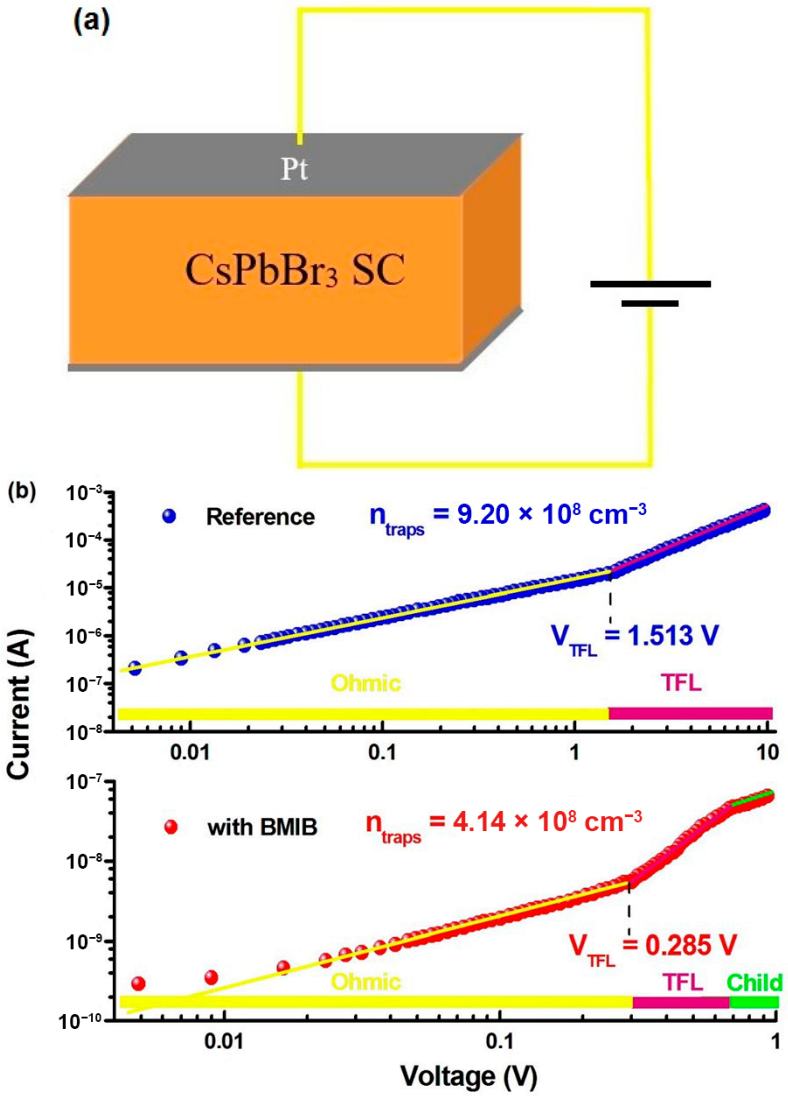

Figure 5. (**a**) Layered structure of the device in schematic form. (**b**) Analysis of space-charge limited current regimes in $CsPbBr_3$ single crystals.

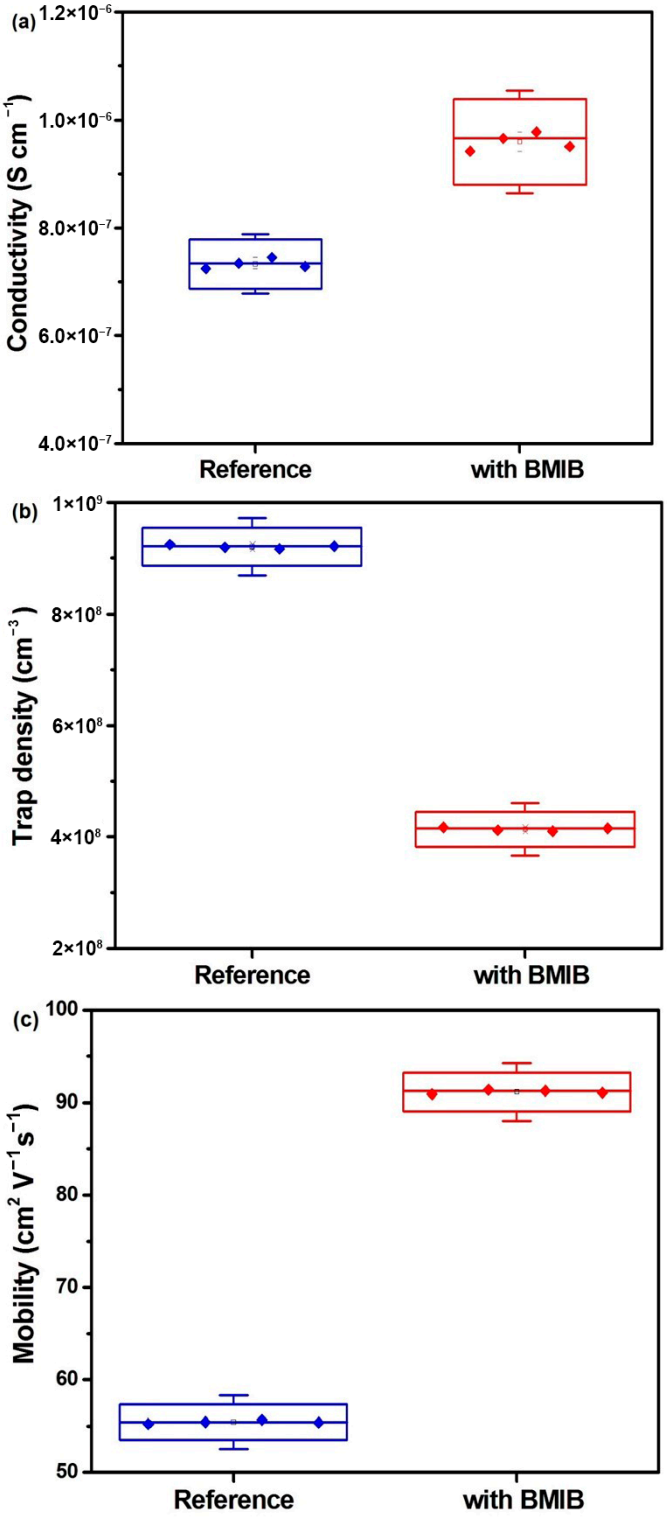

Figure 6. Statistical variations in (**a**) conductivity, (**b**) trap density, and (**c**) mobility of $CsPbBr_3$ single crystals.

To ensure accuracy and reduce measurement errors, we conducted tests on four individual samples of each single crystal type. The η_{trap} was determined to be 9.20 × 10^8 cm^3 for the $CsPbBr_3$ single crystals. In contrast, the $CsPbBr_3$ single crystals prepared using method (2) exhibited a decrease of approximately 45% in trap density, with an average value of 4.14 × 10^8 cm^3 (Figure 6b). The Mott–Gurney law (Equation (3)) can be employed

to determine the carrier mobility (μ) for holes in the investigated $CsPbBr_3$ single crystals. This calculation is based on the analysis of the trap-filled SCLC regions in hole-only devices:

$$\mu = \frac{8J_d L^3}{9\varepsilon\varepsilon_0 V^2} \quad (3)$$

The symbols in this equation maintain their conventional meanings and interpretations. The $CsPbBr_3$ single crystal synthesized using method (2) demonstrates an impressively high average carrier mobility (μ) of 91.43 cm^2/Vs, which is more than twice the value calculated for the reference $CsPbBr_3$ single crystal (55.51 cm^2/Vs) (Figure 6c). This outcome aligns with our expectations. The exceptional quality of the $CsPbBr_3$ single crystal synthesized using method (2) is evident through its ultralow trap density and remarkably high carrier mobility.

TRPL spectroscopy was employed to investigate the recombination dynamics of photoexcited species in both single crystals. The decay curves were analyzed using a bi-exponential decay model, which includes both a fast component (τ_1) and a slow component (τ_2). The fast decay component (τ_1) can be attributed to nonradiative recombination resulting from surface defects, while the slow decay component (τ_2) is associated with bulk radiative recombination. Figure 7a illustrates that the $CsPbBr_3$ single crystal synthesized using method (2) has a longer carrier lifetime (τ_1 = 4 ns and τ_2 = 37 ns) compared to the reference $CsPbBr_3$ single crystal (τ_1 = 3 ns and τ_2 = 22 ns). It is evident that the $CsPbBr_3$ single crystal fabricated using method (2) exhibits longer fast and slow components, indicating an increase in both surface and bulk nonradiative recombination within this crystal type [36]. Upon examination, it becomes evident that the discrepancy between carrier lifetimes is quite insignificant, and their values may fluctuate depending on various conditions (measurement time, wavelength, etc.). Analysis of the decay curves revealed the presence of three distinct decay times: two occurring rapidly and one exhibiting a slower decay rate. Figure 7b displays the statistical distributions of the mean rapid and slow components corresponding to each crystal. Upon examining the statistical distributions in Figure 7b, it is evident that the average fast component is nearly identical for both types of single crystals. However, the slow component is longer for the $CsPbBr_3$ single crystal (2), which indicates a decrease in bulk nonradiative recombination within it.

Utilizing the calculated values of μ and τ, it is possible to estimate the diffusion length (L_D) for both single crystal by employing Equation (4):

$$L_D = \sqrt{(k_B T/e) \times \mu\tau} \quad (4)$$

The symbols in this equation maintain their conventional meanings and interpretations.

For the $CsPbBr_3$ single crystal (2), the average L_D values, derived from the rapid and gradual components of the carrier lifetime, are 1.88 ± 0.24 μm and 0.48 ± 0.08 μm. In comparison, the reference $CsPbBr_3$ single crystal exhibits corresponding values of 0.87 ± 0.11 μm and 0.23 ± 0.04 μm, as illustrated in Figure 7c. The L_D values observed in the $CsPbBr_3$ single crystal (2) are twice as large as those found in the reference $CsPbBr_3$ single crystal. This discrepancy suggests an enhanced quality and improved optoelectronic properties in the former.

The performance of optoelectronic devices, particularly single-crystal-based photodetectors, largely depends on the quality and optoelectronic properties of the active material used in their construction. With possession of a superior-quality $CsPbBr_3$ single crystal, we proceeded to create planar-type photodetectors by applying Pt electrodes onto the surfaces of both single crystals (refer to Section 2.3). Initially, we gathered the I-V characteristics under conditions of darkness, as depicted in Figure 8a. It is evident that photodetector (2) displays an elevated dark current (I_d) compared to that of photodetector (1). The elevated I_d observed could be indicative of a heightened density of defects within the $CsPbBr_3$ single crystal (2) [29,31]. Nonetheless, our findings indicate that the single crystal (2) exhibits lower η_{trap} values than the reference $CsPbBr_3$ single crystal (Figure 6b). Consequently, we

associate the higher dark current (I_d) with the hole mobility and enhanced conductivity of single crystal (2). To confirm the quality of the photodetectors, an assessment was conducted by examining the photocurrent under light and with an applied bias. It was observed that the photocurrent (I_{ph}) rises as the bias increases for all photodetector types, with photodetector (2) displaying a higher Iph compared to photodetector (1).

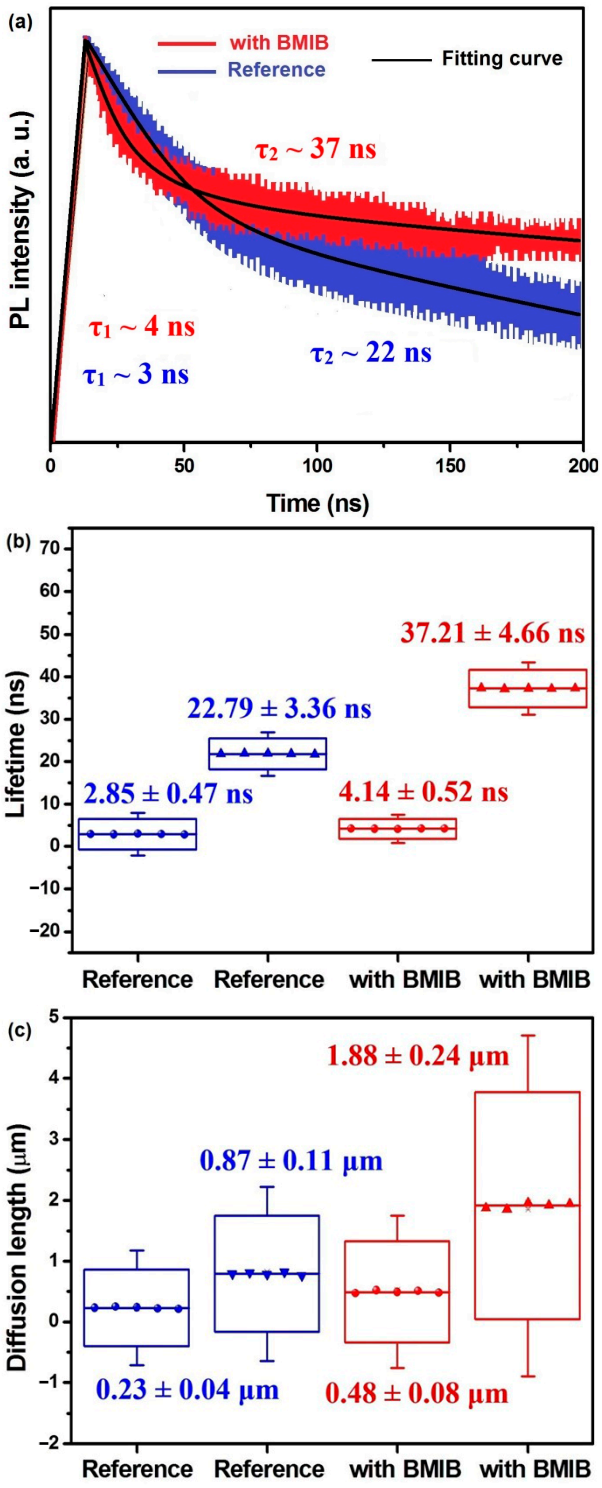

Figure 7. (**a**) Comparative photoluminescence decay analysis of $CsPbBr_3$ single crystals (RT). Statistical variations in (**b**) carrier lifetime and (**c**) diffusion length of $CsPbBr_3$ single crystals.

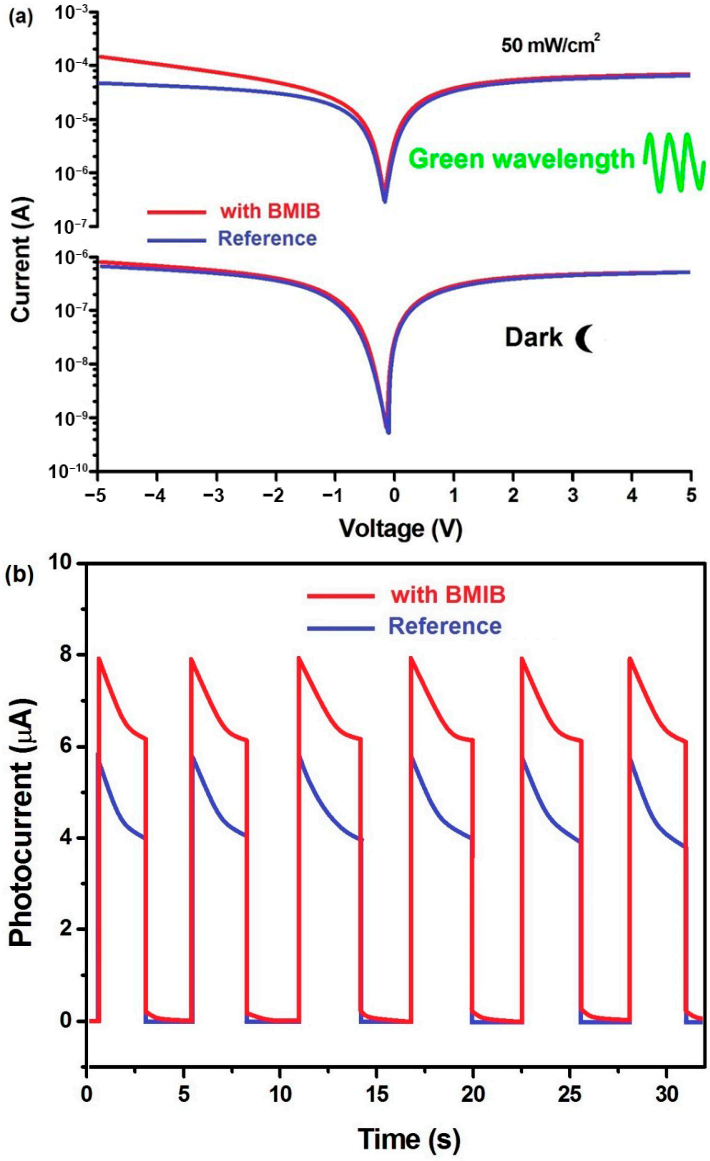

Figure 8. (**a**) Current–voltage characterization under illumination and dark conditions. (**b**) Time-dependent current response.

Given the well-documented hysteretic behavior in halide perovskites attributed to ion migration [37], this study investigated the influence of BMIB on photodetector hysteresis. To gain a deeper understanding of the efficiency of the photodetectors, we conducted measurements of the transient photoresponses for both devices. Figure 8b presents the current–time (I-t) characteristics of each photodetector type, as measured at an irradiance power of 10^{-3} W/cm^2. The prominent, sharp peaks followed by a gradual decay of photocurrent over an extended time period, as observed in both current–time (I-t) curves, can potentially be attributed to the prevailing influence of charge recombination and ion accumulation near the electrode. This occurs while the impact of carrier trapping under λ_G is considered minimal [38]. Photodetector (2) exhibited a significantly larger photocurrent, suggesting more efficient separation of photogenerated charges likely due to reduced non-radiative recombination processes. Figure 9a illustrates the relationship between incident light intensity and photocurrent density on a logarithmic scale (J_{ph}) for each photodetector. This dependence signifies a rise in J_{ph} with increasing light intensity, likely due to an enhanced rate of photogenerated charge carriers. It is worth noting that photodetector (2) produced nearly 35% higher J_{ph} compared to photodetector (1), indicating its enhanced

performance capabilities. The R, D*, and EQE values of the examined device were determined using Equations (S3), (S4), and (S5), respectively. These calculations can be found in Supplementary Note 2. As shown in Figure 9b, photodetector (2) demonstrates superior responsivity (R) and external quantum efficiency (EQE) compared to photodetector (1). The maximum R and EQE values for photodetector (2) reach 5.37 A W^{-1} and 0.97, respectively, while photodetector (1) exhibits values of 4.30 A W^{-1} and 0.83, respectively, under a green light with an intensity of 10^{-3} W/cm^2. Nevertheless, there was no substantial difference observed in the values of specific detectivity. Furthermore, the increased dark current (I_d) of photodetector (2) did not have a considerable impact on the general functioning of the photodetectors. Photodetector (2) exhibits enhanced photodetection characteristics partly due to its increased diffusion length (L_D). This L_D parameter significantly influences the extraction of photogenerated charge carriers, ultimately impacting the photodetector's responsivity [39].

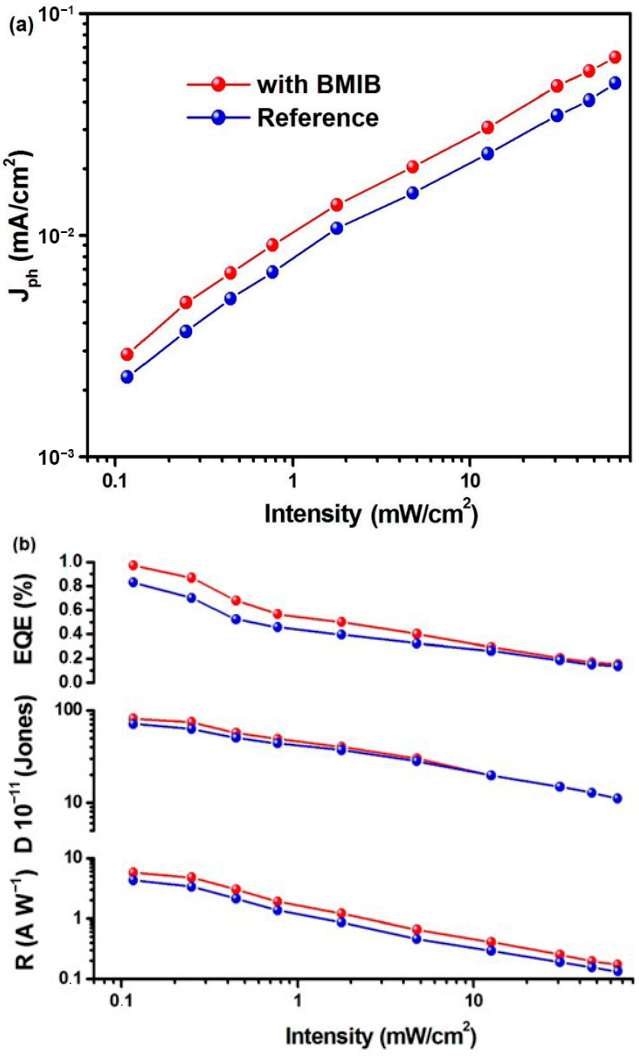

Figure 9. *Cont.*

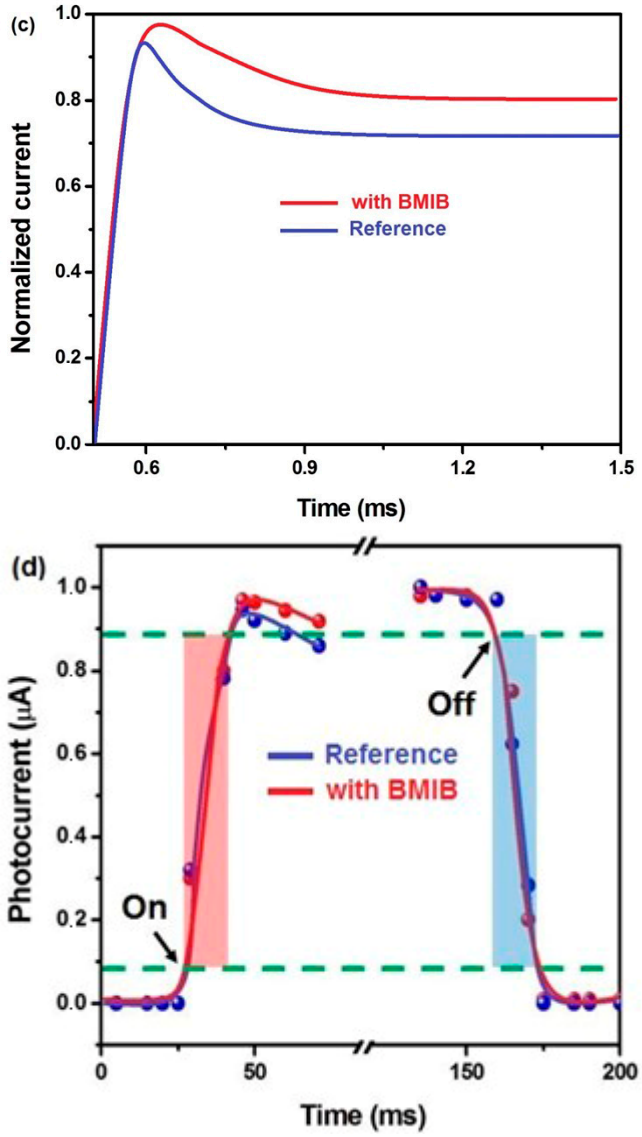

Figure 9. (**a**) J_{ph} characterization under varied light intensity. (**b**) The parameters R, D*, and EQE under varied light intensity. (**c**) Normalized photocurrent transient at 2 V (green light). (**d**) Comparative photoresponse kinetics of reference and BMIB-treated PDs under green light.

Analysis of the transient photoresponse decay for each photodetector under green light and bias voltage can provide valuable insights into charge recombination and ion movement within the devices [38]. We investigated the transient photocurrent decay behavior of each photodetector type under 10^{-3} W/cm^2 irradiance power. The normalized spectra are presented in Figure 9c. The slower decay of photocurrent observed in photodetector (2) under green light illumination suggests a reduced rate of charge recombination and ion movement compared to photodetector (1). A photodetector's response time reflects its ability to track fast-changing light signals. Figure 9d presents the rise time (τ_{on}, 10% to 90% of saturation) and fall time (τ_{off}, 90% to 10% of saturation) extracted from the normalized photoresponse data for each photodetector type. Photodetector (2) demonstrates a swifter response (rise time τ_{on} = 11.6 ms, fall time τ_{off} = 13.2 ms) compared to photodetector (1) (τ_{on} = 13.8 ms, τ_{off} = 15.4 ms). While this suggests superior conductivity and carrier mobility in photodetector (2), facilitating a more rapid transfer of photogenerated charges, the differences in response times are minimal. Therefore, further statistical analysis on a larger batch of samples would provide more robust confirmation of this behavior and will be considered as a perspective for future work. For photodetectors to be commercially

viable, they must demonstrate reliable performance over extended periods of operation. As illustrated in Figure S1, both photodetectors exhibit remarkable operational stability. After 24 h of continuous operation under a 10^{-3} W/cm^2 light signal, their performance remains around 91% of the initial value, demonstrating stability comparable to findings reported in prior studies [39,40]. The superior photodetector performance achieved with $CsPbBr_3$ single crystal (2) highlights its potential as a highly efficient semiconducting material for optoelectronic device development.

In our study, we observed that the incorporation of BMIB plays a crucial role in reducing the nucleation temperature and enhancing the crystallization process of $CsPbBr_3$. The presence of BMIB likely stabilizes the intermediate species during crystallization, facilitating the formation of $CsPbBr_3$ crystals at lower temperatures. Moreover, BMIB may interact with the Cs^+ ions and Br^- anions, leading to a more homogeneous distribution of these species, which promotes uniform crystal growth. This interaction is crucial in overcoming energy barriers associated with nucleation, ultimately resulting in enhanced crystallinity and reduced defect density in the $CsPbBr_3$ single crystals.

4. Conclusions

In conclusion, our study presents an adapted approach to inverse temperature crystallization, showcasing the cultivation of $CsPbBr_3$ single crystals of superior quality. This achievement was realized by introducing BMIB into the perovskite precursor solution, thereby enabling crystallization at a reduced temperature of 65 °C. The inclusion of BMIB was identified as a catalyst for the self-assembly and crystallization mechanisms, achieved through the creation of $PbBr_2$–ionic liquid complexes. This phenomenon effectively diminishes the crystallization kinetics, thereby promoting the growth of sizable $CsPbBr_3$ single crystals. An investigation into the structural, optical, and electrical characteristics of the $CsPbBr_3$ single crystals synthesized with the assistance of BMIB was conducted and subsequently juxtaposed with those of $CsPbBr_3$ single crystals obtained through the traditional ITC technique at 85 °C. The outcomes indicate that $CsPbBr_3$ single crystals produced with the assistance of BMIB display a higher degree of structural perfection, accompanied by diminished lattice strain, nonradiative recombination, and trap density. These qualities render them appealing for utilization in optoelectronic devices. The device composed of Pt/$CsPbBr_3$/Pt with a planar photodetector structure demonstrated superior characteristics (R = 5.37 A W^{-1} and EQE = 0.97) in comparison to the counterpart relying on the $CsPbBr_3$ single crystal fabricated through the traditional ITC method at 85 °C (method (1)). The exceptional performance can be ascribed to the noted elevated mobility and conductivity inherent in the $CsPbBr_3$ single crystals synthesized by method (1). We hold the perspective that employing a low-temperature ITC technique in cultivating superior $CsPbBr_3$ single crystals will pave the way for the emergence of a novel era in the creation of optoelectronic devices reliant on single crystals.

Supplementary Materials: The following supporting information can be downloaded at: https://www.mdpi.com/article/10.3390/cryst14110956/s1, Figure S1. Photodetector stability under green light in CsPbBr3 with/without BMIB (2 V).

Funding: This research received no external funding.

Data Availability Statement: Data are contained within the article.

Acknowledgments: The researchers would like to thank the Deanship of Graduate Studies and Scientific Research at Qassim University for financial support (QU-APC-2024-9/1).

Conflicts of Interest: The author declares no conflicts of interest.

References

1. López-Fernández, I.; Valli, D.; Wang, C.; Samanta, S.; Okamoto, T.; Huang, Y.; Sun, K.; Liu, Y.; Chirvony, V.S.; Patra, A.; et al. Lead-Free Halide Perovskite Materials and Optoelectronic Devices: Progress and Prospective. *Adv. Funct. Mater.* **2024**, *34*, 2307896. [CrossRef]
2. Gallop, N.P.; Maslennikov, D.; Mondal, N.; Goetz, K.P.; Dai, Z.; Schankler, A.M.; Sung, W.; Nihonyanagi, S.; Tahara, T.; Bodnarchuk, M.I.; et al. Ultrafast vibrational control of organohalide perovskite optoelectronic devices using vibrationally promoted electronic resonance. *Nat. Mater.* **2023**, *23*, 88. [CrossRef] [PubMed]
3. Bechir, M.B.; Alresheedi, F. Electrical and optical investigations lead-free Cesium Bismuth iodide single crystal. *Opt. Mater.* **2024**, *147*, 114621. [CrossRef]
4. Bechir, M.B.; Znaidia, S. Understanding the polaron behavior in $Cs_2CuSbCl_6$ halide double perovskite. *Phys. Chem. Chem. Phys.* **2023**, *25*, 19684. [CrossRef]
5. Niu, G.; Jiang, J.; Wang, X.; Che, L.; Sui, L.; Wu, G.; Yuan, K.; Yang, X. Time-Resolved Dynamics of Metal Halide Perovskite under High Pressure: Recent Progress and Challenges. *J. Phys. Chem. Lett.* **2024**, *15*, 1623. [CrossRef]
6. Bechir, M.B.; Alresheedi, F. Interpretation of dielectric behavior and polaron hopping in lead-free antimony-based double perovskite. *RSC Adv.* **2023**, *13*, 34703. [CrossRef]
7. Hieulle, J.; Krishna, A.; Boziki, A.; Audinot, J.; Farooq, M.; Machado, J.F.; Mladenović, M.; Phirke, H.; Singh, A.; Wirtz, T.; et al. Understanding and decoupling the role of wavelength and defects in light-induced degradation of metal-halide perovskites. *Energy Environ. Sci.* **2024**, *17*, 284. [CrossRef]
8. Emmanuel, M.; Hao, H.; Liu, H.; Jan, A.; Alresheedi, F. Significantly enhanced energy storage density of NNT ceramics using aliovalent Dy^{3+} dopant. *ACS Sustain. Chem. Eng.* **2021**, *9*, 5849–5859. [CrossRef]
9. Liu, C.; Huang, W.; Liu, R. Stable glass-protected CsPbX3 (X = Cl, Br, and I) perovskite quantum dot and their applications in backlight LED. *Prog. Mater. Sci.* **2024**, *143*, 101243. [CrossRef]
10. Alresheedi, F.; Hcini, S.; Bouazizi, M.L.; Boudard, M.; Dhahri, A. Synthesis and study of impendence spectroscopy properties of La0.6Ca0.2Na0.2MnO_3 manganite perovskite prepared using sol–gel method. *J. Mater. Sci. Mater. Electron.* **2020**, *31*, 8248–8257. [CrossRef]
11. Wang, H.; Du, Z.; Jiang, X.; Cao, S.; Zou, B.S.; Zheng, J.; Zhao, J. Ultrastable Photodetectors Based on Blue $CsPbBr_3$ Perovskite Nanoplatelets via a Surface Engineering Strategy. *ACS Appl. Mater. Interfaces* **2024**, *16*, 11694. [CrossRef] [PubMed]
12. Bu, H.; He, C.; Yang, X.; Lu, X.; Liu, X.; Ren, S.; Yi, S.; Chen, L.; Wu, H.; Zhang, G.; et al. Emerging New-Generation Detecting and Sensing of Metal Halide Perovskites. *Adv. Electron. Mater.* **2022**, *8*, 2101204. [CrossRef]
13. Manan, A.; Rehman, M.U.; Faisal, S.; Ullah, A.; Ghazi, Z.A.; Khan, M.A.; Ahmad, A.S.; Alresheedi, F.; Khan, M.A. Simultaneously achievement of high recoverable energy density and efficiency in sodium niobate-based ceramics. *J. Mater. Sci. Mater. Electron.* **2022**, *33*, 22208–22216. [CrossRef]
14. Alresheedi, F. Structure and spectroscopic ellipsometry studies of nanocrystalline Dy_2O_3 thin films deposited on Al_2O3 wafers by electron beam evaporation technique. *J. Mater. Res. Technol.* **2021**, *12*, 2104–2113. [CrossRef]
15. Li, H.; Yu, H.; Wu, D.; Sun, X.; Pan, L. Recent advances in bioinspired vision sensor arrays based on advanced optoelectronic materials. *APL Mater.* **2023**, *11*, 080601. [CrossRef]
16. Alresheedi, F. Superior resistive switching performance in SnO_2 nanoparticles embedded TiO_2 nanorods-based thin films. *Ceram. Int.* **2023**, *49*, 19505–19512. [CrossRef]
17. Duan, Y.; Wang, D.; Costa, R.D. Recent progress on synthesis, characterization, and applications of metal halide perovskites@ metal oxide. *Adv. Funct. Mater.* **2021**, *31*, 2104634. [CrossRef]
18. Zhumekenov, A.A.; Burlakov, V.M.; Saidaminov, M.I.; Alofi, A.S.; Haque, A.; Türedi, B.; Davaasuren, B.; Dursun, İ.; Cho, N.; El-Zohry, A.M.; et al. The role of surface tension in the crystallization of metal halide perovskites. *ACS Energy Lett.* **2017**, *2*, 1782. [CrossRef]
19. Liu, Y.; Sun, J.; Yang, Z.; Yang, D.; Ren, X.; Xu, H.; Yang, Z.; Liu, S. 20-mm-Large single-crystalline formamidinium-perovskite wafer for mass production of integrated photodetectors. *Adv. Opt. Mater.* **2016**, *4*, 1829. [CrossRef]
20. Bechir, M.B.; Alresheedi, F. Growth methods' effect on the physical characteristics of $CsPbBr_3$ single crystal. *Phys. Chem. Chem. Phys.* **2024**, *26*, 1274. [CrossRef]
21. Li, W.; Rao, H.; Chen, B.; Wang, X.; Kuang, D. A formamidinium–methylammonium lead iodide perovskite single crystal exhibiting exceptional optoelectronic properties and long-term stability. *J. Mater. Chem. A Mater. Energy Sustain.* **2017**, *5*, 19431. [CrossRef]
22. Zhao, Y.; Tan, H.; Yuan, H.; Yang, Z.; Fan, J.; Kim, J.; Voznyy, O.; Gong, X.; Quan, L.N.; Tan, C.; et al. Perovskite seeding growth of formamidinium-lead-iodide-based perovskites for efficient and stable solar cells. *Nat. Commun.* **2018**, *9*, 1607. [CrossRef]
23. Nayak, P.K.; Moore, D.T.; Wenger, B.; Nayak, S.; Haghighirad, A.A.; Fineberg, A.; Noel, N.K.; Reid, O.G.; Rumbles, G.; Kukura, P.; et al. Mechanism for rapid growth of organic–inorganic halide perovskite crystals. *Nat. Commun.* **2016**, *7*, 13303. [CrossRef]
24. Liu, Y.; Zhang, Y.; Zhu, X.; Yang, Z.; Ke, W.; Feng, J.; Ren, X.; Zhao, K.; Liu, M.; Kanatzidis, M.G.; et al. Inch-sized high-quality perovskite single crystals by suppressing phase segregation for light-powered integrated circuits. *Sci. Adv.* **2021**, *7*, eabc8844. [CrossRef]
25. Liu, Y.; Zheng, X.; Fang, Y.; Zhou, Y.; Ni, Z.; Xiao, X.; Chen, S.; Huang, J. Ligand assisted growth of perovskite single crystals with low defect density. *Nat. Commun.* **2021**, *12*, 1686. [CrossRef]

26. Wang, F.; Ge, C.; Duan, D.; Lin, H.; Li, L.; Naumov, P.; Hu, H. Recent progress in ionic liquids for stability engineering of perovskite solar cells. *Small Struct.* **2022**, *3*, 2200048. [CrossRef]
27. Wang, Y.; Yang, Y.; Li, N.; Hu, M.; Raga, S.R.; Jiang, Y.; Wang, C.; Zhang, X.; Lira-Cantú, M.; Huang, F.; et al. Ionic liquid stabilized perovskite solar modules with power conversion efficiency exceeding 20%. *Adv. Funct. Mater.* **2022**, *19*, 2204396. [CrossRef]
28. Liu, Y.; Zhang, Y.; Zhao, K.; Yang, Z.; Feng, J.; Zhang, X.; Wang, K.; Meng, L.; Ye, H.; Liu, M.; et al. A 1300 mm^2 ultrahigh-performance digital imaging assembly using high-quality perovskite single crystals. *Adv. Mater.* **2018**, *30*, 1707314. [CrossRef]
29. Zia, W.; Aranda, C.; Pospı, J.; Rai, M.; Momblona, C.; Gorji, S.; Muñoz-Matutano, G.; Saliba, M. Impact of Low-Temperature Seed-Assisted Growth on the Structural and Optoelectronic Properties of $MAPbBr_3$ Single Crystals. *Chem. Mater.* **2023**, *35*, 5458. [CrossRef]
30. Liu, Y.; Zhang, Y.; Yang, Z.; Feng, J.; Xu, Z.; Li, Q.; Hu, M.; Ye, H.; Zhang, X.; Liu, M.; et al. Low-temperature-gradient crystallization for multi-inch high-quality perovskite single crystals for record performance photodetectors. *Mater. Today* **2019**, *22*, 67. [CrossRef]
31. Cho, Y.; Jung, H.Y.; Kim, Y.S.; Kim, Y.; Park, J.; Yoon, S.; Lee, Y.; Cheon, M.; Jeong, S.Y.; Jo, W. High speed growth of $MAPbBr_3$ single crystals via low-temperature inverting solubility: Enhancement of mobility and trap density for photodetector applications. *Nanoscale* **2021**, *13*, 8275. [CrossRef]
32. Zhang, S.; Xiao, T.; Fadaei-Tirani, F.; Scopelliti, R.; Nazeeruddin, M.K.; Zhu, D.; Dyson, P.J.; Fei, Z. The chemistry of the passivation mechanism of perovskite films with ionic liquids. *Inorg. Chem.* **2022**, *61*, 5010. [CrossRef]
33. Amari, S.; Verilhac, J.; D'Aillon, E.G.; Ibanez, A.; Zaccaro, J. Optimization of the growth conditions for high quality $CH_3NH_3PbBr_3$ hybrid perovskite single crystals. *Cryst. Growth Des.* **2020**, *20*, 1665. [CrossRef]
34. Mahapatra, A.; Prochowicz, D.; Kruszyńska, J.; Satapathi, S.; Akın, S.; Kumari, H.; Kumar, P.; Fazel, Z.; Tavakoli, M.M.; Yadav, P. Effect of bromine doping on the charge transfer, ion migration and stability of the single crystalline MAPb $(Br_xI_{1-x})_3$ photodetector. *J. Mater. Chem. C* **2021**, *9*, 15189. [CrossRef]
35. Kalam, A.; Runjhun, R.; Mahapatra, A.; Tavakoli, M.M.; Trivedi, S.; Dastjerdi, H.T.; Kumar, P.; Lewiński, J.; Pandey, M.K.; Prochowicz, D.; et al. Interpretation of resistance, capacitance, defect density, and activation energy levels in single-crystalline MAPbI3. *J. Phys. Chem. C* **2020**, *124*, 3496. [CrossRef]
36. Murali, B.; Yengel, E.; Yang, C.; Peng, W.; Alarousu, E.; Bakr, O.M.; Mohammed, O.F. The surface of hybrid perovskite crystals: A boon or bane. *ACS Energy Lett.* **2017**, *2*, 846. [CrossRef]
37. Meloni, S.; Moehl, T.; Tress, W.; Franckevic, M.; Saliba, M.; Lee, Y.H.; Gao, P.; Nazeeruddin, M.K.; Zakeeruddin, S.M.; Rothlisberger, U.; et al. Ionic polarization-induced current–voltage hysteresis in CH3NH3PbX3 perovskite solar cells. *Nat. Commun.* **2016**, *7*, 10334. [CrossRef]
38. Mahapatra, A.; Anilkumar, V.; Nawrocki, J.; Pandey, S.V.; Chavan, R.D.; Yadav, P.; Prochowicz, D. Transient Photocurrent Response in a Perovskite Single Crystal-Based Photodetector: A Case Study on the Role of Electrode Spacing and Bias. *Adv. Electron. Mater.* **2023**, *9*, 2300226. [CrossRef]
39. Mahapatra, A.; Anilkumar, V.; Chavan, R.D.; Yadav, P.; Prochowicz, D. Understanding the origin of light intensity and temperature dependence of photodetection properties in a $MAPbBr_3$ single-crystal-based photoconductor. *ACS Photonics* **2023**, *10*, 1424. [CrossRef]
40. Gavranovic, S.; Pospisil, J.; Zmeskal, O.; Novak, V.; Vanysek, P.; Castkova, K.; Cihlar, J.; Weiter, M. Electrode spacing as a determinant of the output performance of planar-type photodetectors based on methylammonium lead bromide perovskite single crystals. *ACS Appl. Mater. Interfaces* **2022**, *14*, 20159. [CrossRef]